

Learning-based Axial Video Motion Magnification

Kwon Byung-Ki¹, Oh Hyun-Bin², Kim Jun-Seong², Hyunwoo Ha², Tae-Hyun Oh^{1,2,3}

¹Graduate School of AI, POSTECH ²Department of Electrical Engineering, POSTECH

³Institute for Convergence Research and Education in Advanced Technology, Yonsei University

{byungki.kwon, hyunbinoh, junseong.kim,
hyunwooha, taehyun}@postech.ac.kr

Abstract

Video motion magnification amplifies invisible small motions to be perceptible, which provides humans with a spatially dense and holistic understanding of small motions in the scene of interest. This is based on the premise that magnifying small motions enhances the legibility of motions. In the real world, however, vibrating objects often possess convoluted systems that have complex natural frequencies, modes, and directions. Existing motion magnification often fails to improve legibility since the intricate motions still retain complex characteristics even after being magnified, which may distract us from analyzing them. In this work, we focus on improving legibility by proposing a new concept, axial motion magnification, which magnifies decomposed motions along the user-specified direction. Axial motion magnification can be applied to various applications where motions of specific axes are critical, by providing simplified and easily readable motion information. To achieve this, we propose a novel Motion Separation Module that enables to disentangle and magnify the motion representation along axes of interest. Furthermore, we build a new synthetic training dataset for the axial motion magnification task. Our proposed method improves the legibility of resulting motions along certain axes by adding a new feature: user controllability. Axial motion magnification is a more generalized concept; thus, our method can be directly adapted to the generic motion magnification and achieves favorable performance against competing methods. Our project page is available at <https://axial-momag.github.io/axial-momag/>.

1. Introduction

Motions are always present in our surroundings. Among them, small motions often convey important signals in practical applications, *e.g.*, building structure health monitoring [4–8, 27], machinery fault detection [28, 32, 38], sound recovery [9], and healthcare [1, 2, 11, 16, 23]. Video motion magnification [20, 24, 39, 40, 42] is the technique to amplify subtle motions in a video, revealing details of motion that are hard to perceive with the naked eyes. This allows users to grasp spatially dense and holistic behavior information of the scene of interest instantly, as long as the resulting motion is simple and easily interpretable. However, in practice, vibrating objects in the real world often possess complex systems that have complex natural frequencies, modes, and directions [25]. Even after being magnified, the intricate movement within a video persists, which restricts the advantages of motion magnification because the key underlying premise of its effectiveness is based on the legibility of the magnified motion in aforementioned applications, *i.e.*, effectively understanding the way objects move.

In this work, we focus on improving the legibility of magnified motion by proposing a novel concept, *axial* motion magnification, which magnifies decomposed motions along the user-specified direction. All the existing works, *e.g.*, [17, 24, 26, 31, 39, 40, 42], have overlooked this key importance of the legibility according to axes in practice. There are many practical cases where the importance of motion varies according to axes. For example, in the fault detection application of machines in Fig. 1, even small motions along the vulnerable axis are critical while bigger and dominant rotational motions are not [22]. Likewise, many apparatus consisting of natural or artificial materials often have vulnerable axes due to the asymmetry property of microstructures, *e.g.*, fracture toughness [3, 18, 37]. This motivates us to separately analyze motions according to axes.

Specifically, we propose a novel learning-based axial motion magnification method, where the motions in a user-specified axis are magnified. Our method can independently magnify small motions along two orthogonal orientation axes with

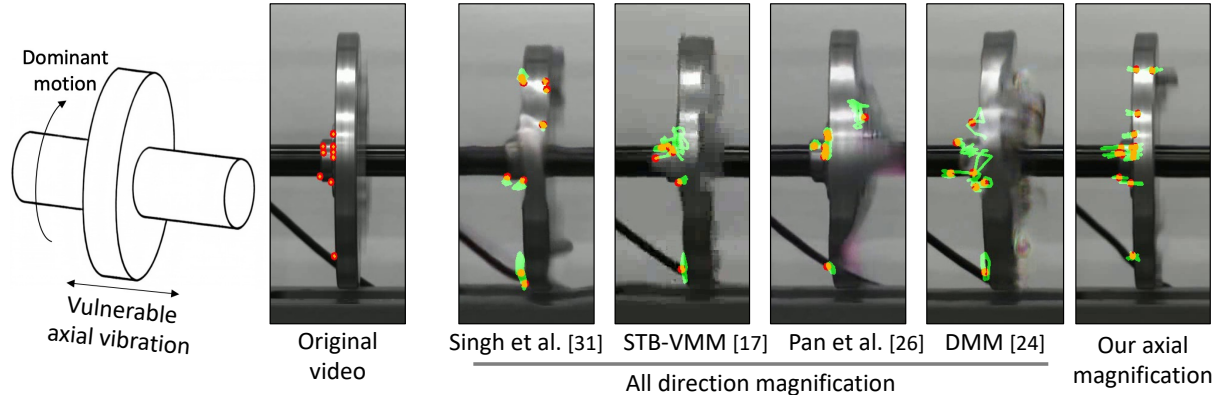


Figure 1. **Importance of axial motion magnification.** When identifying faults in rotating machinery, analysis of the vulnerable axial vibration is critical [22]. Existing learning-based methods [17, 24, 26, 31] amplify motions along all axes, which yield artifacts. It hinders the analyses of vulnerable axial vibration. This motivates the importance of our axial motion magnification that magnifies decomposed motions along a user-specified axis. We magnify the axial vibration only, achieving artifact-free results and the legibility of critical motions. For the visualization purpose, we overlay the sample trajectories obtained from the Kanade-Lucas-Tomasi (KLT) Tracker [21].

two independent magnification factors for each axis, which facilitates the analysis of complex small motions in the lens of axes favorable to the user. To this end, we propose the Motion Separation Module (MSM) that disentangles the motion representation into two orthogonal orientations and manipulates it into the direction specified by the user. For training the proposed neural network, we develop and build a new synthetic dataset for the axial motion magnification task. Thereby, our proposed approach adds a new user control feature, which improves the legibility of resulting motions along a certain axis. This allows our axial motion magnification becomes a generalization of the existing *generic* motion magnification. Thus, our method can be directly adopted to the generic motion magnification task and achieve favorable performance against competing methods. We summarize our main contributions as follows:

- We propose the new concept, learning-based axial motion magnification, which allows us to selectively amplify small motions along a specific direction.
- We propose and analyze the Motion Separation Module (MSM) for the axial motion magnification. We find that adopting the MSM is effective in not only axial magnification but also distinguishing small motions from noise.
- We propose the way to synthesize a new synthetic dataset to train the new axial motion magnification model.

2. Related Work

Liu *et al.* [20] first pioneered the video motion magnification task, which involves estimating explicit motion trajectory via optical flow, known as the Lagrangian representation [42], to generate magnified frames. They group and filter the motion trajectories based on motion similarity and user’s intervention, and magnify them through explicit image warping, followed by video inpainting to fill holes created by the explicit warping.

Wu *et al.* [42] re-formulate the motion magnification task as an Eulerian method that represents motion by intensity changes of pixels at each fixed location without actual movement [12]. The Eulerian approach, *e.g.*, [24, 33–36, 39, 40, 42, 43], becomes standard in motion magnification due to its noise robustness, sensitivity to small motions, and simple system by avoiding challenging warp and inpaint approach for filling holes and handling occlusions. The system of the Eulerian methods typically consists of motion representation, manipulation, and reconstruction. The previous works can be categorized into two main focuses: 1) proposing motion representations or 2) motion manipulation methods.

In the first category, Wu *et al.* [42] present the motion representation motivated by the first-order Taylor expansion, which is implemented by Laplacian pyramid as spatial decomposition. Wadhwa *et al.* [39, 40] enhance the representation by modeling the motion as phase representations, which are implemented by complex steerable filters [29] in [39] and Riesz transform in [40] as spatial decomposition, respectively. These works rely on the classic signal processing theory with such hand-designed spatial filter designs, which do not model non-linear phenomena such as occlusion or disocclusion of objects. This yields artifacts and noisy results, especially in object boundaries.

To deal with, Oh *et al.* [24] first coined learning-based video motion magnification, called Deep Motion Magnification (DMM), by modeling motion representation with deep neural networks. As no real data exists for training video motion magnification, they propose a method to build motion magnification synthetic data. With the development, other learning-based variants [17, 31] have been proposed, focusing on neural network architectures. These approaches demonstrate promising results by effectively handling diverse challenging scenarios such as occlusion and noisy inputs. Also, the motion magnification factors of the data-driven approaches can be controlled by the way the synthetic dataset is generated, while those of the traditional methods [39, 42] are theoretically restricted.

In the second category, when Wu *et al.* [42] present Eulerian motion magnification, they also propose to use a temporal filter on the motion representation to select the motion frequency of interest. This allows to suppress the noise by focusing on specific motions as well as increasing the legibility of magnified motion. There were attempts to extend to increase the legibility by proposing temporal filters to magnify different types of motions and deal with artifacts from large motions: acceleration [33, 43], intensity-aware temporal filter [36], velocity or all-frequency filter [24]. Our work is compatible with all these methods.

In this work, we present a new notion of motion magnification by disentangling motion axes of the user’s interest. We design a neural architecture to induce disentanglement of motion in oriented axes. Also, to train such a model, we propose the synthetic data generation pipeline for the axial motion magnification task. In contrast to all the existing Eulerian methods, which overlook the directional legibility of the resulting magnified motions, we add a novel feature to motion magnification.

3. Learning-based Axial Motion Magnification

In this section, we first briefly discuss preliminaries about generic motion magnification, which refers to the methods that amplify the motion regardless of motion direction, including the prior arts [17, 24, 26, 31, 42] (Sec. 3.1). Then, we re-frame the motion magnification problem in the view of axial motion magnification (Sec. 3.2), and elaborate on our network architecture, and synthetic data generation method (Sec. 3.3).

3.1. Preliminary – Generic Motion Magnification

Following the convention [39, 42], for simplicity, we consider the 1D image intensity being shifted by the displacement function $\delta(x, t)$ which is parameterized by position x and time t . It can be generalized to local translational motion in 2D image [42]. Given an underlying intensity profile function $f(\cdot)$, the 1D image intensity $I(x, t)$ can be represented as

$$I(x, t) = f(x + \delta(x, t)). \tag{1}$$

The goal of motion magnification is to synthesize the magnified image $\hat{I}(x, t)$:

$$\hat{I}(x, t) = f(x + (1 + \alpha)\delta(x, t)), \tag{2}$$

where α denotes the magnification factor. The key factor of motion magnification methods lies in the extraction of the displacement function $\delta(x, t)$ from Eq. (1). If $\delta(x, t)$ can be decomposed, we can approximate $\hat{I}(x, t)$ by multiplying $\delta(x, t)$ with the magnification factor α and applying the reverse of the decomposition process. However, it is ill-posed problem to extract exact displacements from the observed intensity images [42]. Instead, the prior arts approximately decompose $\delta(x, t)$; for example, Wu *et al.* [42] use the first-order Taylor expansion as:

$$I(x, t) \approx f(x) + \delta(x, t) \frac{\partial f(x)}{\partial x}. \tag{3}$$

Learning-based methods [17, 24, 31] design neural networks that have intermediate representations related to $\delta(\cdot)$, called shape representation. The representations are multiplied by α , followed by reconstruction for magnification.

3.2. Axial Motion Magnification

To introduce the axial motion magnification task, we now consider the 2D spatial coordinate by slightly abusing the notations, *e.g.*, $\mathbf{x} = (x, y)$ to refer to the coordinate in the 2D image intensity $I(\mathbf{x}, t)$.

Problem Definition. We can represent $I(\mathbf{x}, t) = f(\mathbf{x} + \delta(\mathbf{x}, t))$ with a 2D displacement vector $\delta(\mathbf{x}, t) \in \mathbb{R}^2$. Given an angle $\phi \in \mathbb{R}$ of the user-specified direction of interest, the goal of the axial motion magnification task is to isolate and amplify the motion component corresponding to the direction angle ϕ within the displacement vector. We represent the axially magnified image $\hat{I}^\phi(\mathbf{x}, t)$ as

$$\hat{I}^\phi(\mathbf{x}, t) = f(\mathbf{x} + \alpha^\phi \delta^\phi(\mathbf{x}, t)), \tag{4}$$

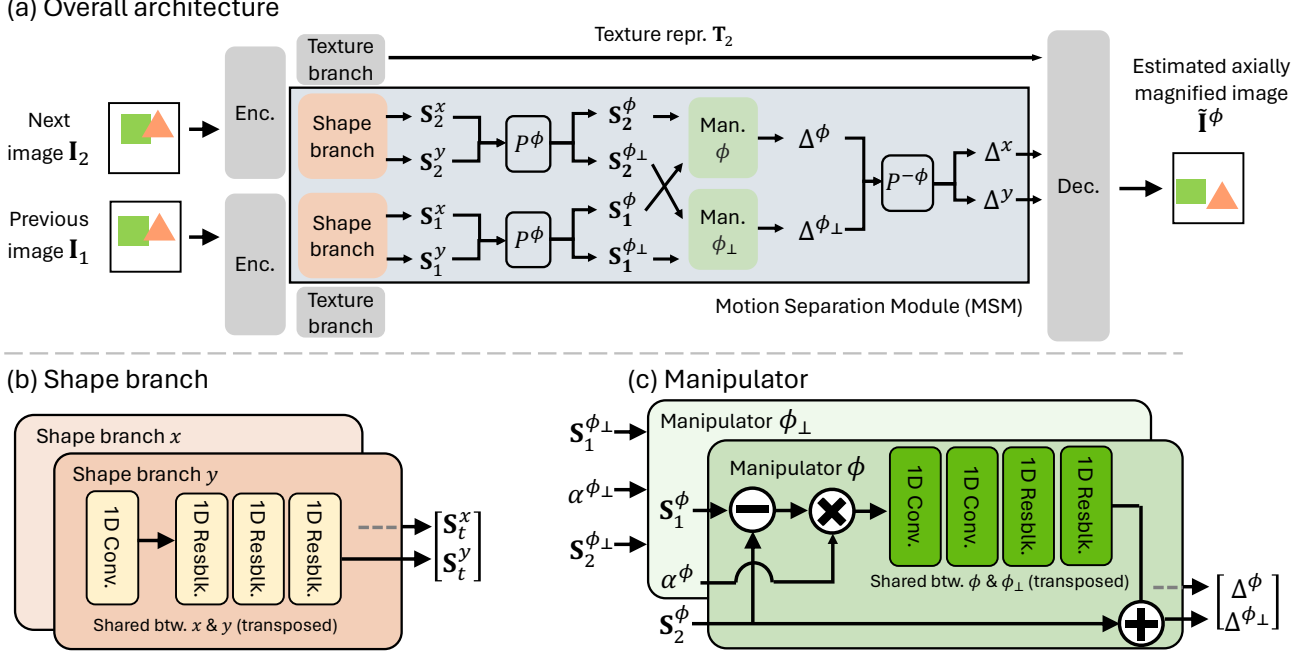


Figure 2. **Proposed architecture.** (a) The *Encoder* outputs features from input images and the features are fed to the *Texture* branch and *Motion Separation Module (MSM)*. (b) Using weight-shared 1D convolutions, the *Shape* branch extracts shape representations along the x and y -axes. These representations are fed to the projection layer P^ϕ , which generates axial shape representations, *i.e.*, S_t^ϕ and $S_t^{\phi_\perp}$. (c) the *Manipulator* amplifies them by the axial magnification factors and the inverse projection layer $P^{-\phi}$ re-project them onto the x and y -axes. Finally, the *Decoder* predicts the axially magnified image from the outputs from both the *Texture* branch and *MSM*.

where $\alpha^\phi \geq 0$ denotes the axial magnification factor and $\delta^\phi(\mathbf{x}, t)$ the projection of $\delta(\mathbf{x}, t)$ onto a 2D directional unit vector \mathbf{p}^ϕ with the angle ϕ , *i.e.*, the motion component. We can break down the motion component $\delta^\phi(\mathbf{x}, t)$ into:

$$\delta^\phi(\mathbf{x}, t) = \text{proj}_{\mathbf{p}^\phi} \delta(\mathbf{x}, t). \quad (5)$$

Relationship with Generic Motion Magnification. If we obtain $\delta(\mathbf{x}, t)$, we can determine $\delta^\phi(\mathbf{x}, t)$ and $\delta^{\phi_\perp}(\mathbf{x}, t)$ through the projections onto \mathbf{p}^ϕ and \mathbf{p}^{ϕ_\perp} . In this case, we can extend Eq. 4 to represent not only the displacement vector of an angle $\delta^\phi(\mathbf{x}, t)$ but also of its orthogonal direction $\delta^{\phi_\perp}(\mathbf{x}, t)$, as

$$\hat{I}^\phi(\mathbf{x}, t) = f(\mathbf{x} + \alpha^\phi \delta^\phi(\mathbf{x}, t) + \alpha^{\phi_\perp} \delta^{\phi_\perp}(\mathbf{x}, t)), \quad (6)$$

where $\alpha_\phi, \alpha_{\phi_\perp} \geq 0$ denotes the axial magnification factors corresponding to the ϕ and ϕ_\perp directions, respectively. This formulation encompasses the various motion magnification scenarios, *e.g.*, axial and generic motion magnifications. Setting α^{ϕ_\perp} to 0 leads to the formulation resulting in axial motion magnification, while setting α^ϕ equal to α^{ϕ_\perp} results in generic motion magnification.

3.3. Neural Networks and Training

Departing from the previous learning-based methods that are confined to generic motion magnification [17, 24, 26, 31], we introduce a novel neural network architecture and a dedicated training dataset designed to learn two angle-aware motion representations proportional to the motion displacement δ^ϕ and δ^{ϕ_\perp} , respectively. These allow our approach to unveil a distinctive feature: the magnification of motion in user-defined directions while retaining the functionality for generic motion magnification.

Network Architecture. Our whole architecture consists of *Encoder*, *Texture & Shape* branches, *Manipulator*, and *Decoder* similar to DMM [24] (see Fig. 2-(a)), where texture represents color and texture-related information while shape represents scene structure-related information that later leads to motion δ [24]. To extract axial shape representations, we design

Motion Separation Module (MSM) consisting of the completely re-designed and dedicated *Shape* branch and *Manipulator* as depicted in Fig. 2-(b,c). In MSM, instead of extracting a single specified direction’s δ^ϕ , we design to extract its orthogonal direction’s δ^{ϕ_\perp} as well. This design choice is motivated by the extended axial motion magnification equation Eq. 6 and enables conducting various motion magnifications, including both axial and generic motion magnifications.

Given consecutive input video frames $\mathbf{I}_t \in \mathbb{R}^{H \times W \times 3}$ at $t = 1$ and $t = 2$ for example, texture representations $\mathbf{T}_t \in \mathbb{R}^{H/4 \times W/4 \times 32}$ are obtained by $\mathbf{T}_t = F(E(\mathbf{I}_t))$, where $E(\cdot)$ and $F(\cdot)$ denote the *Encoder* and the *Texture* branch, respectively. The outputs of E are fed into MSM. The same output from E is fed into the *Texture* branch and MSM, respectively.

To extract the motion representations along two orthogonal orientations and manipulate them based on the user-defined angle, we grant the learnable parameters to learn the directionality in MSM. Our *Shape* branch $G(\cdot)$ first extracts the axial shape representations along the canonical x and y -axes by applying weight-shared 1D convolutions but with spatially transposing the convolution kernels, yielding $[\mathbf{S}_t^x, \mathbf{S}_t^y] = G(E(\mathbf{I}_t))$ where $\mathbf{S}_t^x, \mathbf{S}_t^y \in \mathbb{R}^{H/2 \times W/2 \times 32}$. Then, these are projected by the *projection* layer, which produces axial shape representations of ϕ and ϕ_\perp directions, *i.e.*, \mathbf{S}_t^ϕ and $\mathbf{S}_t^{\phi_\perp}$. Motivated by the steerable filters [13], where an arbitrarily rotated representation can be synthesized by a linear combination of directional representations, we design the projection layer P^ϕ with a linear matrix as

$$P^\phi \left(\begin{bmatrix} \mathbf{S}_t^x \\ \mathbf{S}_t^y \end{bmatrix} \right) = \begin{bmatrix} \cos \phi & \sin \phi \\ -\sin \phi & \cos \phi \end{bmatrix} \begin{bmatrix} \mathbf{S}_t^x \\ \mathbf{S}_t^y \end{bmatrix} = \begin{bmatrix} \mathbf{S}_t^\phi \\ \mathbf{S}_t^{\phi_\perp} \end{bmatrix}. \quad (7)$$

The *Manipulator* $M(\cdot)$ computes the difference of the axial shape representations and magnifies them by multiplying the axial magnification factors α^ϕ . Then, these manipulated representations are fed into subsequent 1D convolutions, and added to the axial shape representation \mathbf{S}_2^ϕ . For ϕ_\perp , we use the same manipulator, of which weights are shared but spatially transposed, for applying α^{ϕ_\perp} . Note that, with this separation of ϕ and ϕ_\perp , we can set the magnification factors α^ϕ and α^{ϕ_\perp} independently, enabling broad applications of controls as another benefit. For the outputs of the *Manipulator* $\Delta^\phi, \Delta^{\phi_\perp}$, where $\Delta^\phi = M(\mathbf{S}_1^\phi, \mathbf{S}_2^\phi, \alpha^\phi)$, we re-project them onto the canonical x and y -axes by inverse projection layer $P^{-\phi}$, obtaining Δ^x, Δ^y . Finally, the *Decoder* $D(\cdot)$ predicts the axially magnified output frame $\tilde{\mathbf{I}}^\phi$ as

$$\tilde{\mathbf{I}}^\phi = D(\mathbf{T}_2, \Delta^x, \Delta^y). \quad (8)$$

This network architecture enables the network to conduct both generic and axial motion magnification, given the user setting of the angle ϕ . The model is trained with the loss function suggested by DMM [24] with a slight modification to impose the loss separately to the x -axis and y -axis shape representations. Details of the loss function can be found in the supplementary material.

Training Data Generation. In the real world, acquiring consecutive images and magnified images at the same time is impossible. Due to this, DMM [24] proposes a synthetic training dataset for the generic motion magnification task. However, this dataset is not sufficient to induce the disentanglement of the axial property we need. Thus, we propose a new synthetic dataset specifically designed for the axial motion magnification, where the motion between \mathbf{I}_1 and $\hat{\mathbf{I}}^\phi$ is associated with the angle ϕ and axial magnification factor vector $\alpha = (\alpha^\phi; \alpha^{\phi_\perp})$. Motivated by the synthetic dataset generation protocol of DMM, we synthesize the training data pairs using the widely adopted simple copy-paste method [14, 24].

Figure 3 shows the synthetic data generation pipeline. We sample one background from COCO [19] and $K-1$ number of foreground textures with segmentation masks from PASCAL VOC [10]. These elements are randomly located on image planes of resolution 384×384 to produce K previous layer images $\{\mathbf{I}_1^k\}_{k=1}^K$ and corresponding masks $\{\Omega_1^k\}_{k=1}^K$. Following this, with randomly sampled K translation parameters $\{\mathbf{d}^k\}_{k=1}^K$, we generate the next layer images $\{\mathbf{I}_2^k\}_{k=1}^K$ and masks $\{\Omega_2^k\}_{k=1}^K$ by translating the initial layers and masks according to $\{\mathbf{d}^k\}_{k=1}^K$. For the axially magnified layer images $\{\hat{\mathbf{I}}^{\phi,k}\}_{k=1}^K$ and their masks $\{\hat{\Omega}^{\phi,k}\}_{k=1}^K$, we sample K axial magnification vectors $\{\alpha^k\}_{k=1}^K$ and a single degree of angle ϕ . Then, we perform the same procedure as the next layers but with the axially magnified translation parameters $\{\alpha^k(\text{proj}_{\mathbf{p}^\phi} \mathbf{d}^k; \text{proj}_{\mathbf{p}^\perp} \mathbf{d}^k)\}_{k=1}^K$. These previous, next, and axially magnified layer images and masks are then superimposed into a single image to yield $\mathbf{I}_1, \mathbf{I}_2$, and $\hat{\mathbf{I}}^\phi$, respectively. Our dataset also includes the angle ϕ and the object-wise magnification map Λ which is generated by superimposing $\{\alpha^k\}_{k=1}^K$ segmented with $\{\Omega_1^k\}_{k=1}^K$. We observe that utilizing both ϕ and Λ are useful for learning the representations distinguishing small motions from noises, which will be discussed on Sec. 4.3. Additionally, the adaptation of both ϕ and Λ enables pixel-wise axial motion magnification. We provide more details in the supplementary materials.

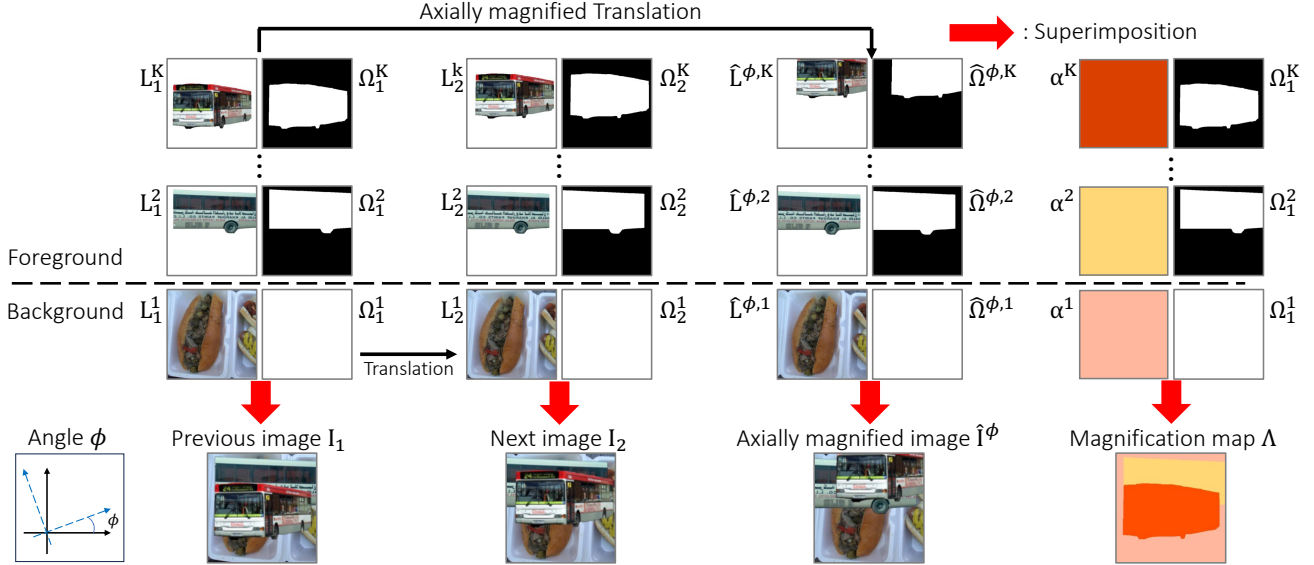


Figure 3. **Synthetic data generation pipeline for axial motion magnification.** From the sampled background and foregrounds, each with their own segmentation masks, we compose the previous layer images $\{\mathbf{L}_1^k\}_{k=1}^K$ and masks $\{\Omega_1^k\}_{k=1}^K$. To generate next layer images $\{\mathbf{L}_2^k\}_{k=1}^K$ and masks $\{\Omega_2^k\}_{k=1}^K$, we apply the random translations to $\{\mathbf{L}_1^k\}_{k=1}^K$ and $\{\Omega_1^k\}_{k=1}^K$. Axially magnified layer images $\{\hat{\mathbf{L}}^{\phi,k}\}_{k=1}^K$ and masks $\{\hat{\Omega}^{\phi,k}\}_{k=1}^K$ are also synthesized by translations but with the axially magnified translation parameters. These images and masks are then superimposed into a single image to yield \mathbf{I}_1 , \mathbf{I}_2 , and $\hat{\mathbf{I}}^\phi$, respectively. The dataset also include angles ϕ and the object-wise magnification maps Λ generated by superimposing $\{\alpha^k\}_{k=1}^K$ with $\{\Omega_1^k\}_{k=1}^K$.

4. Experiments

Implementation Details. We train our learning-based axial motion magnification network on the newly proposed dataset, which contains a total of 100k samples, for 50 epochs with a batch size of 8 and a learning rate 2×10^{-4} .

Evaluation Setup. We examine the performance of our method in axial and generic motion magnification, respectively. In generic motion magnification, we compare our method to the phase-based method [39], Singh *et al.* [31], STB-VMM [17], Pan *et al.* [26], and DMM [24]. In axial motion magnification, there is no method of handling a user-specified angle and performing axial magnification due to our novel problem setup. Therefore, we propose a new axial baseline, called *modified phase-based*, by modifying Wadhwa *et al.* [39]. Specifically, we modulate the phase-based to operate in axial scenario by employing a half-octave bandwidth pyramid and two orientations, with one of them having its phase representation manipulated along the axis of interest. We use both the *dynamic* and *static* modes in the experiments following DMM [24]. Additional experiments of diverse scenarios and implementation details can be found in the supplementary material and video, including the magnified results with the temporal bandpass filters separating the motion with the frequency of interest.

4.1. Axial Motion Magnification

We evaluate our method compared to the modified phase-based method in the axial motion magnification scenario, to demonstrate the effectiveness of the learning-based axial motion magnification.

Qualitative Results. We demonstrate the advantage of our method that it can amplify only the motion along the axis of interest while disentangling the motions in uninterested directions that interfere with motion analysis. To illustrate this concept concretely, consider a scenario where a shaft is rotating in the radial direction. In such cases, magnifying and examining the motion along the axial direction, which is crucial to assess the condition of the rotating machinery [22], becomes challenging due to the dominance of rotational motion over the axial component. We conduct an experiment shown in Fig. 4 by attaching weights to a rotor to impose an imbalance, which results in axial vibrations. Then, we acquire a video of the imbalanced rotor, called *rotor imbalance* sequence. We choose a horizontal-axis line in the original frame and visualize x - t slices for the magnified output frames from each method, respectively. Note that we also provide the result of DMM [24] as a reference to compare the results of axial motion magnification with generic motion magnification. As

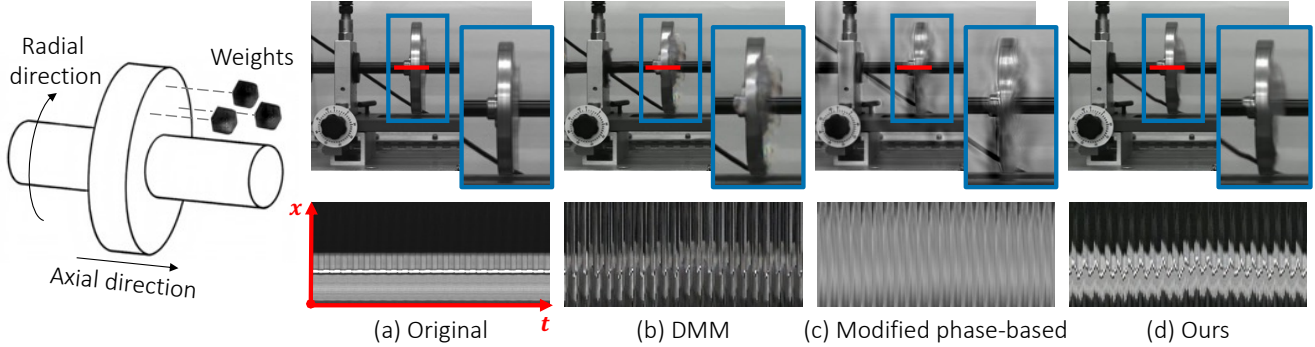


Figure 4. **[Left] Imposing an imbalance on a rotor, [Right] Qualitative results in axial motion magnification scenario.** We attach weights to a rotor to impose an imbalance and acquire *rotor imbalance* sequence, which has axial vibrations. Then, we amplify only the motion of rotor’s axial direction with the magnification factor $\alpha = 40$, using ours and modified phase-based method. We also show the magnified result of DMM [24] as a reference result of generic motion magnification. Our method generates magnified frames without artifacts and exhibits the x - t slice showing clearly legible axial vibrations, while modified phase-based method and DMM both suffer from severe artifacts and have unclear axial vibrations in the x - t slice.

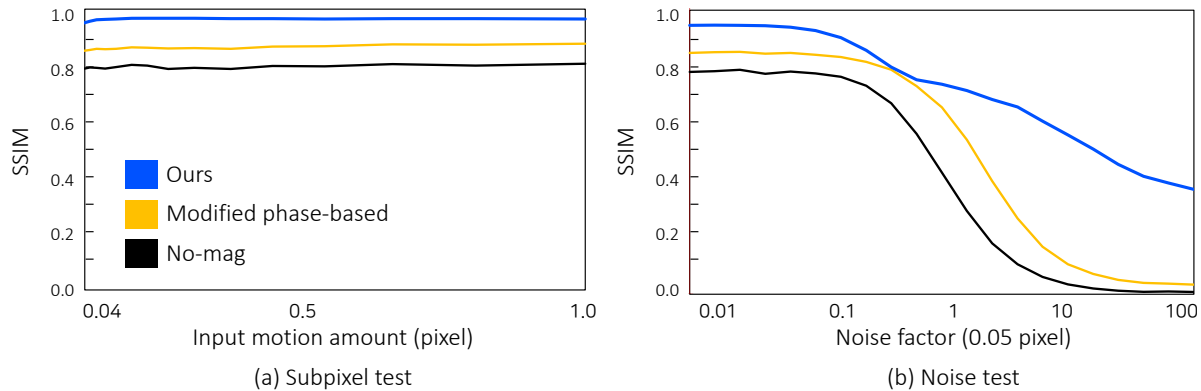


Figure 5. **Quantitative results in axial motion magnification scenario.** (a) In the subpixel test, ours shows superior performance on SSIM over the modified phase-based method across all input motion amount, ranging from 0.04 to 1.0. (b) In the noise tests when the input motion amount is 0.05 pixel, we observe a growing disparity in SSIM scores between ours and the phase-based approach, as the noise factor rises.

shown in Fig. 4, our method produces the magnified output frames without artifacts and exhibits the x - t slice that clearly depicts axial vibrations. In contrast, the modified phase-based method suffers from severe ringing artifacts, likely due to the overcompleteness of the complex steerable filter [29, 30], which cannot perfectly separate the phase representation into two orthogonal directions. DMM yields the magnified frames with artifacts and unclear axial vibrations in the x - t slice, since the representation of generic motion magnification method struggles to disentangle the dominant motion of the radial direction from the motion of interest, *i.e.*, axial direction’s motion.

Quantitative Results. To quantitatively evaluate our learning-based axial motion magnification method, we generate an axial evaluation dataset based on the validation dataset of DMM [24]. The method of generating the dataset is almost the same as that of the training dataset. One difference is that we adjust the motion amplification factor to ensure that the amplified motion magnitude along a random axis is equal to 10. The motion amplification factor for the other axis is set to half the value. Note that we set ϕ to be 0 for this quantitative evaluation. We report the Structural Similarity Index (SSIM) [41] between the ground truth and output frames of the modified phase-based method and ours. As a reference, we provide the SSIM between ground truth and input frames. Figure 5 summarizes the results. We measure the SSIM by varying the levels of motion (Fig. 5-(a) Subpixel test) and additive noise (Fig. 5-(b) Noise test) in the input images. The number of evaluation data samples for each level of motion and noise is 1,000. Regardless of the input motion magnitude and noise level, our method consistently outperforms the modified phase-based approach, which indicates that our proposed network architecture

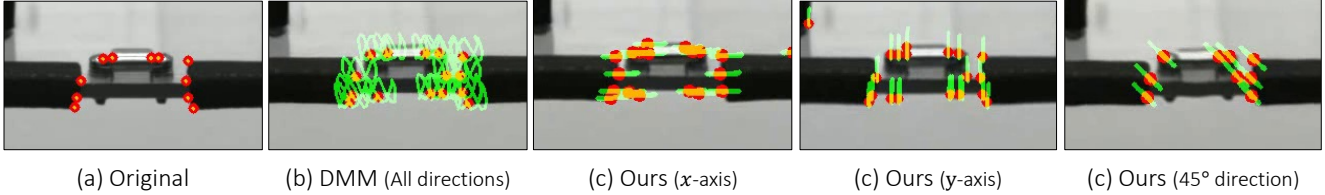


Figure 6. **Motion legibility improvement.** We visualize the $40\times$ magnified frames of the structure, which are overlaid with the sampled trajectories from the KLT tracker. Ours shows simplified and legible motion trajectories when magnifying along the specific axis (*i.e.*, x -axis, y -axis or diagonal-axis in this case), while DMM [24] produces the trajectories that are more complex and hard to interpret.

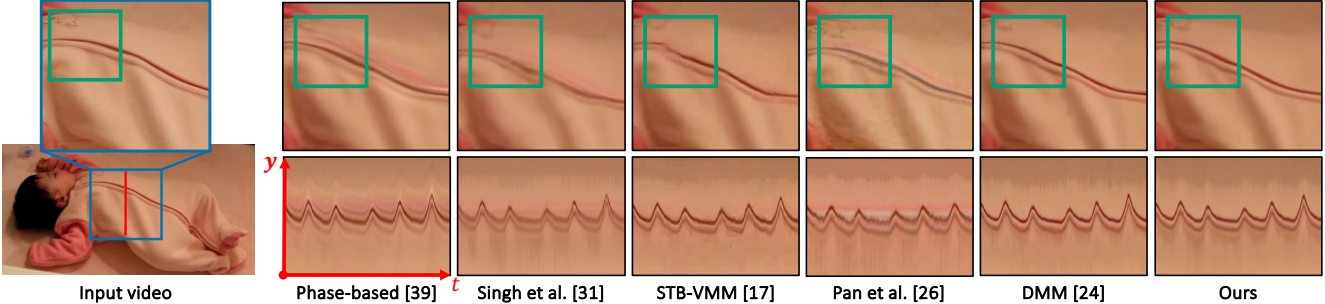


Figure 7. **Qualitative results in generic motion magnification scenario.** We amplify the *baby* sequence with the magnification factor $\alpha=20$, using phase-based method [39], learning-based methods [17, 24, 26, 31], and Ours. Ours and DMM favorably preserve the edges of the clothes and show no ringing artifacts in the magnified frames and the x - t slices. In contrast, the magnified output frames of the phase-based, Singh *et al.*, STB-VMM, and Pan *et al.* show ringing artifacts or blurry results.

and dataset are effective for learning axis-wise disentangled representations.

Motion Legibility Comparison. To demonstrate the improved legibility of magnified motions by our method, we use a structure that exhibits complex movements. We then visualize and compare the motion trajectories, tracked by the KLT tracker, of the $40\times$ magnified video sequences of this structure using both the generic method (DMM) [24] and the axial method (Ours). As shown in Fig. 6, our method shows legible trajectories when magnifying along the specific axis (*i.e.*, x -axis, y -axis or diagonal-axis in this case), while DMM shows the entangled trajectories difficult to judge major motion characteristics.

4.2. Generic Motion Magnification

Our method can be readily adapted for generic motion magnification scenarios without further training. This adaptability is achieved by simply multiplying the same magnification factors with the axis-wise shape representations. In the context of generic motion magnification, we compare our method with the phase-based method [39] and the learning-based methods [17, 24, 26, 31].

Qualitative Results. We visualize the magnified output frames and plot the x - t slices for the *baby* sequence, comparing ours with the several motion magnification methods in the generic scenarios (see Fig. 7). Both our method and DMM [24] favorably preserve the edges of the baby’s clothing and show no ringing artifacts in the magnified results of breathing motion. In contrast, the phase-based method [39], Singh *et al.* [31], STB-VMM [17], Pan *et al.* [26] and show severe ringing artifacts or blurry results¹.

Quantitative Results. To quantitatively verify the ability of our method in generic motion magnification, we synthesize a generic validation dataset. Unlike the axial case, we set the magnification factor α to be identical along the x and y axes. As shown in Fig. 8, we report SSIM [41] between ground truth and output frames from the phase-based method [39] and the learning-based methods [17, 24, 26, 31]. For input motion ranges from 0.04 to 1.0, ours outperforms the phase-based method, Singh *et al.* [31], Pan *et al.* [26]. Compared to DMM [24] and STB-VMM [17], ours demonstrates favorable performance,

¹We reproduced all the results using the codes publicly accessible.

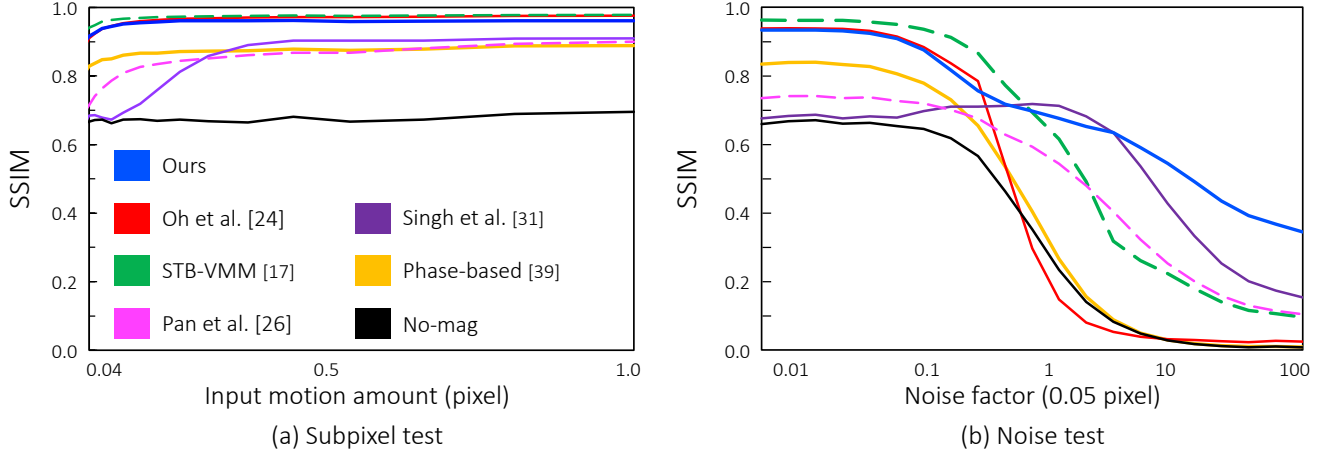


Figure 8. **Quantitative results in generic motion magnification scenario.** (a) In the subpixel test, Ours outperforms phase-based method, Singh *et al.*, and Pan *et al.* and achieves favorable performance on SSIM compared to DMM and STB-VMM. (b) In the noise test, Ours shows comparable noise tolerance compared to other methods and high noise tolerance as the noise factor increases.

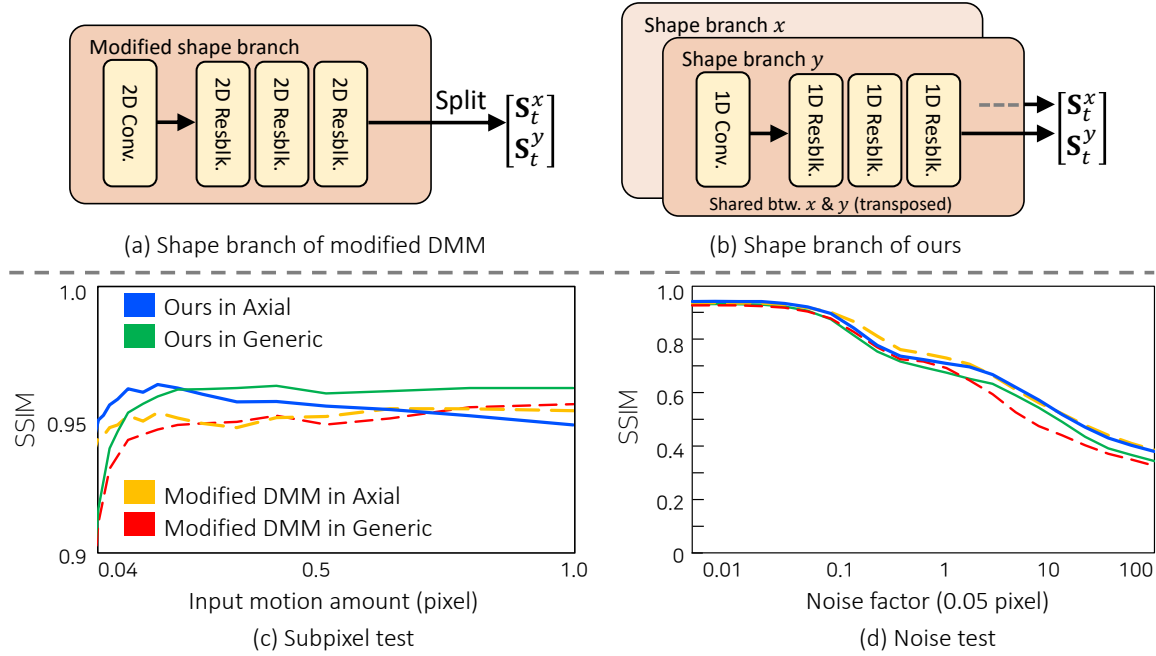


Figure 9. **[Top] Architectural difference on the *shape* branch, [Bottom] Quantitative results of ablating Motion Separation Module (MSM).** (a) The modified DMM, designed for ablation study, employs 2D convolutions and splits features along channel dimensions for axial motion magnification. (c) Ours with MSM generally achieves higher SSIM in the subpixel test on generic and axial evaluation datasets. (d) In the noise test, Ours shows comparable performance to the modified DMM.

which exceeds the threshold for visually acceptable SSIM scores [15]. Ours demonstrates comparable noise tolerance to other methods and exhibits high noise tolerance as noise factor increases.

4.3. Ablation Study

In this section, we conduct ablation studies to evaluate the impact of the Motion Separation Module (MSM) and the components of the proposed synthetic training data. We carry out quantitative experiments on the evaluation dataset of both the generic case and the axial case that has random angles.

Motion Separation Module (MSM). To validate the effectiveness of MSM, we design a competitor called modified DMM, which closely resembles that of DMM [24]. As shown in the top of Fig. 9, different from our method that uses 1D convolu-

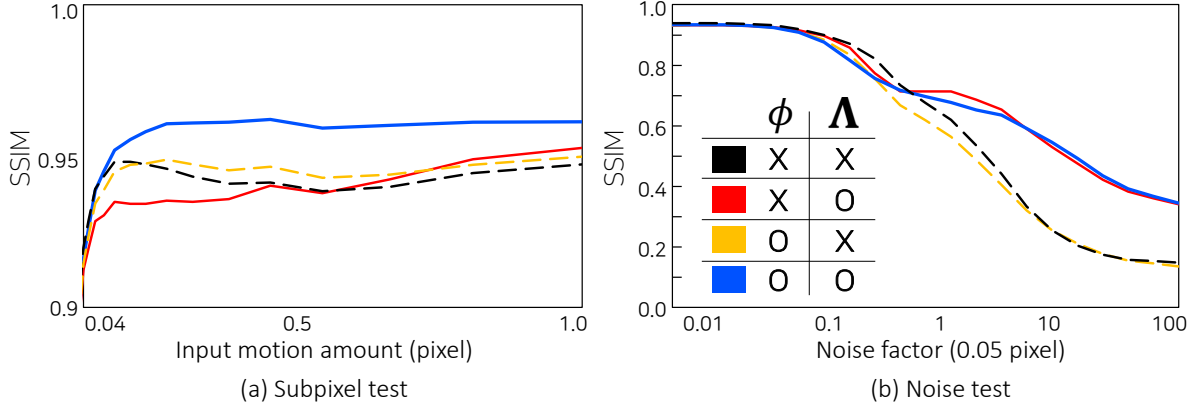


Figure 10. **Ablation study of the components in data generation in the generic evaluation dataset.** We generate the different training data varying the presence of the angle ϕ and the object-wise motion magnification map Λ , and evaluate the networks trained on each dataset configuration using the generic evaluation dataset. (a) Using both ϕ and Λ demonstrates best performance in the subpixel test. (b) In the noise test, we observe that utilizing Λ notably enhances noise tolerance.

tions, the modified DMM employs 2D convolutions in the *Shape* branch and the *Manipulator*. The axial shape representations of the modified DMM are acquired by dividing the feature map along the channel dimension. We train the networks with the same loss function and training details as Ours. The bottom of Fig. 9 shows that Ours with MSM generally achieves higher SSIM in the subpixel test on the generic and axial evaluation datasets. These results show the effectiveness of the MSM in capturing small motions. In the noise test, Ours shows comparable performance to the modified DMM.

Components of Synthetic Training Data. To evaluate the impact of the angle ϕ and the object-wise motion magnification map Λ , we generate the different types of training data varying the presence of these components. Our newly designed dataset incorporates both ϕ and Λ , contrasting with the dataset that follows the same setup as DMM [24], which does not contain either element. In addition, we generate two more datasets that each add one of these components (*i.e.*, either ϕ or Λ) to the base dataset that initially does not include them. Note that evaluating the networks trained on these datasets on the axial evaluation dataset is infeasible since the networks trained without ϕ cannot perform axial motion magnification. Thus, we use the generic evaluation dataset for this ablation study. Fig. 10 shows that the addition of either ϕ or Λ achieves no improvement in the subpixel test. The combined use of both ϕ and Λ yields the most significant performance improvement in the subpixel test, demonstrating that our proposed data set is beneficial in the generic motion magnification task as well. In the noise test, utilizing Λ notably enhances noise tolerance, while the addition of ϕ has no effect on noise tolerance.

5. Conclusion

In this work, we present a novel concept, axial motion magnification, which improves the legibility of the motions by disentangling and magnifying the motion representations along axes specified by users. To this end, we propose an innovative learning-based approach for both axial and generic motion magnification, incorporating the Motion Separation Module (MSM) to effectively extract and magnify motion representations along two orthogonal orientations. To support this, we establish a new synthetic data generation pipeline tailored for axial motion magnification. Our proposed method provides user controllability and significantly enhances the legibility of the motions along chosen axes, showing favorable performance compared to competing methods, even in cases of generic motion magnification. Although axial motion magnification serves as one branch that enhances user convenience, another branch can be the method to perform motion magnification in real-time, which is useful and beneficial for various applications. Similarly to DMM, our method falls short of real-time performance for 720p videos, presenting an avenue for future research in this area.

References

- [1] Guha Balakrishnan, Fredo Durand, and John Guttag. Detecting pulse from head motions in video. In *Proceedings of the IEEE conference on computer vision and pattern recognition*, pages 3430–3437, 2013. [1](#)
- [2] Biagio Brattoli, Uta Büchler, Michael Dorkenwald, Philipp Reiser, Linard Filli, Fritjof Helmchen, Anna-Sophia Wahl, and Björn Ommer. Unsupervised behaviour analysis and magnification (ubam) using deep learning. *Nature Machine Intelligence*, 3(6):495–506, 2021. [1](#)
- [3] NR Brodnik, Stella Brach, CM Long, G Ravichandran, B Bourdin, KT Faber, and K Bhattacharya. Fracture diodes: Directional asymmetry of fracture toughness. *Physical Review Letters*, 126(2):025503, 2021. [1](#)
- [4] Y-J Cha, Justin G Chen, and Oral Büyüköztürk. Output-only computer vision based damage detection using phase-based optical flow and unscented kalman filters. *Engineering Structures*, 132:300–313, 2017. [1](#)
- [5] Justin G Chen, Neal Wadhwa, Young-Jin Cha, Frédo Durand, William T Freeman, and Oral Buyukozturk. Structural modal identification through high speed camera video: Motion magnification. In *Topics in Modal Analysis I, Volume 7: Proceedings of the 32nd IMAC, A Conference and Exposition on Structural Dynamics, 2014*, pages 191–197. Springer, 2014.
- [6] Justin G Chen, Neal Wadhwa, Young-Jin Cha, Frédo Durand, William T Freeman, and Oral Buyukozturk. Modal identification of simple structures with high-speed video using motion magnification. *Journal of Sound and Vibration*, 345:58–71, 2015.
- [7] Justin G Chen, Neal Wadhwa, Frédo Durand, William T Freeman, and Oral Buyukozturk. Developments with motion magnification for structural modal identification through camera video. In *Dynamics of Civil Structures, Volume 2*, pages 49–57. Springer, 2015.
- [8] Justin G Chen, Abe Davis, Neal Wadhwa, Frédo Durand, William T Freeman, and Oral Büyüköztürk. Video camera-based vibration measurement for civil infrastructure applications. *Journal of Infrastructure Systems*, 23(3):B4016013, 2017. [1](#)
- [9] Abe Davis, Michael Rubinstein, Neal Wadhwa, Gautham J Mysore, Fredo Durand, and William T Freeman. The visual microphone: Passive recovery of sound from video. *ACM Transactions on Graphics (SIGGRAPH)*, 2014. [1](#)
- [10] Mark Everingham, Luc Van Gool, Christopher KI Williams, John Winn, and Andrew Zisserman. The pascal visual object classes (voc) challenge. *International journal of computer vision*, 88(2):303–338, 2010. [5](#), [1](#)
- [11] Wenkang Fan, Zhuohui Zheng, Wankang Zeng, Yinran Chen, Hui-Qing Zeng, Hong Shi, and Xiongbiao Luo. Robotically surgical vessel localization using robust hybrid video motion magnification. *IEEE Robotics and Automation Letters*, 6(2):1567–1573, 2021. [1](#)
- [12] William T Freeman, Edward H Adelson, and David J Heeger. Motion without movement. *ACM SIGGRAPH*, 25(4):27–30, 1991. [2](#)
- [13] William T Freeman, Edward H Adelson, et al. The design and use of steerable filters. *IEEE Transactions on Pattern analysis and machine intelligence*, 13(9):891–906, 1991. [5](#), [2](#)
- [14] Golnaz Ghiasi, Yin Cui, Aravind Srinivas, Rui Qian, Tsung-Yi Lin, Ekin D Cubuk, Quoc V Le, and Barret Zoph. Simple copy-paste is a strong data augmentation method for instance segmentation. In *Proceedings of the IEEE/CVF conference on computer vision and pattern recognition*, pages 2918–2928, 2021. [5](#)
- [15] Hyunwoo Ha, Oh Hyun-Bin, Kim Jun-Seong, Kwon Byung-Ki, Kim Sung-Bin, Linh-Tam Tran, Ji-Yun Kim, Sung-Ho Bae, and Tae-Hyun Oh. Revisiting learning-based video motion magnification for real-time processing, 2024. [9](#)
- [16] Mirek Janatka, Hani J Marcus, Neil L Dorward, and Danail Stoyanov. Surgical video motion magnification with suppression of instrument artefacts. In *Medical Image Computing and Computer Assisted Intervention—MICCAI 2020: 23rd International Conference, Lima, Peru, October 4–8, 2020, Proceedings, Part III 23*, pages 353–363. Springer, 2020. [1](#)
- [17] Ricard Lado-Roigé and Marco A Pérez. Stb-vmm: Swin transformer based video motion magnification. *Knowledge-Based Systems*, 269:110493, 2023. [1](#), [2](#), [3](#), [4](#), [6](#), [8](#)
- [18] Beichen Li, Bolei Deng, Wan Shou, Tae-Hyun Oh, Yuanming Hu, Yiyue Luo, Liang Shi, and Wojciech Matusik. Computational discovery of microstructured composites with optimal strength-toughness trade-offs. *arXiv preprint arXiv:2302.01078*, 2023. [1](#)
- [19] Tsung-Yi Lin, Michael Maire, Serge Belongie, James Hays, Pietro Perona, Deva Ramanan, Piotr Dollár, and C Lawrence Zitnick. Microsoft coco: Common objects in context. In *European Conference on Computer Vision (ECCV)*, 2014. [5](#), [1](#)
- [20] Ce Liu, Antonio Torralba, William T Freeman, Frédo Durand, and Edward H Adelson. Motion magnification. *ACM transactions on graphics (TOG)*, 24(3):519–526, 2005. [1](#), [2](#)
- [21] Bruce D Lucas and Takeo Kanade. An iterative image registration technique with an application to stereo vision. In *IJCAI’81: 7th international joint conference on Artificial intelligence*, pages 674–679, 1981. [2](#), [4](#)
- [22] Yin Luo, Wenqi Zhang, Yakun Fan, Yuejiang Han, Weimin Li, and Emmanuel Acheaw. Analysis of vibration characteristics of centrifugal pump mechanical seal under wear and damage degree. *Shock and Vibration*, 2021:1–9, 2021. [1](#), [2](#), [6](#)
- [23] Ernesto Moya-Albor, Jorge Brieva, Hiram Ponce, and Lourdes Martínez-Villaseñor. A non-contact heart rate estimation method using video magnification and neural networks. *IEEE Instrumentation & Measurement Magazine*, 23(4):56–62, 2020. [1](#)
- [24] Tae-Hyun Oh, Ronnachai Jaroensri, Changil Kim, Mohamed Elgharib, Frédo Durand, William T Freeman, and Wojciech Matusik. Learning-based video motion magnification. In *Proceedings of the European Conference on Computer Vision (ECCV)*, pages 633–648, 2018. [1](#), [2](#), [3](#), [4](#), [5](#), [6](#), [7](#), [8](#), [9](#), [10](#)
- [25] G Oliveto, Adolfo Santini, and E Tripodi. Complex modal analysis of a flexural vibrating beam with viscous end conditions. *Journal of Sound and Vibration*, 200(3):327–345, 1997. [1](#)

- [26] Zhaoying Pan, Daniel Geng, and Andrew Owens. Self-supervised motion magnification by backpropagating through optical flow. *Advances in Neural Information Processing Systems*, 36, 2024. [1](#), [2](#), [3](#), [4](#), [6](#), [8](#)
- [27] Qiwen Qiu and Denvin Lau. Defect detection in frp-bonded structural system via phase-based motion magnification technique. *Structural Control and Health Monitoring*, 25(12):e2259, 2018. [1](#)
- [28] Aral Sarrafi, Zhu Mao, Christopher Niezrecki, and Peyman Poozesh. Vibration-based damage detection in wind turbine blades using phase-based motion estimation and motion magnification. *Journal of Sound and vibration*, 421:300–318, 2018. [1](#)
- [29] Eero P Simoncelli and William T Freeman. The steerable pyramid: A flexible architecture for multi-scale derivative computation. In *Proceedings., International Conference on Image Processing*, pages 444–447. IEEE, 1995. [2](#), [7](#)
- [30] Eero P Simoncelli, William T Freeman, Edward H Adelson, and David J Heeger. Shiftable multiscale transforms. *IEEE transactions on Information Theory*, 38(2):587–607, 1992. [7](#)
- [31] Jasdeep Singh, Subrahmanyam Murala, and G Kosuru. Multi domain learning for motion magnification. In *Proceedings of the IEEE/CVF Conference on Computer Vision and Pattern Recognition*, pages 13914–13923, 2023. [1](#), [2](#), [3](#), [4](#), [6](#), [8](#)
- [32] Michał Śmieja, Jarosław Mamala, Krzysztof Prażnowski, Tomasz Ciepliński, and Łukasz Szumilas. Motion magnification of vibration image in estimation of technical object condition-review. *Sensors*, 21(19):6572, 2021. [1](#)
- [33] Shoichiro Takeda, Kazuki Okami, Dan Mikami, Megumi Isogai, and Hideaki Kimata. Jerk-aware video acceleration magnification. In *IEEE Conference on Computer Vision and Pattern Recognition (CVPR)*, 2018. [2](#), [3](#), [10](#)
- [34] Shoichiro Takeda, Yasunori Akagi, Kazuki Okami, Megumi Isogai, and Hideaki Kimata. Video magnification in the wild using fractional anisotropy in temporal distribution. In *IEEE Conference on Computer Vision and Pattern Recognition (CVPR)*, 2019.
- [35] Shoichiro Takeda, Megumi Isogai, Shinya Shimizu, and Hideaki Kimata. Local riesz pyramid for faster phase-based video magnification. *IEICE Transactions on Information and Systems.*, 103(10):2036–2046, 2020.
- [36] Shoichiro Takeda, Kenta Niwa, Mariko Isogawa, Shinya Shimizu, Kazuki Okami, and Yushi Aono. Bilateral video magnification filter. In *IEEE Conference on Computer Vision and Pattern Recognition (CVPR)*, 2022. [2](#), [3](#)
- [37] MT Tilbrook, K Rozenburg, ED Steffler, L Rutgers, and M Hoffman. Crack propagation paths in layered, graded composites. *Composites Part B: Engineering*, 37(6):490–498, 2006. [1](#)
- [38] Kiran Vernekar, Hemantha Kumar, and KV Gangadharan. Gear fault detection using vibration analysis and continuous wavelet transform. *Procedia Materials Science*, 5:1846–1852, 2014. [1](#)
- [39] Neal Wadhwa, Michael Rubinstein, Frédo Durand, and William T Freeman. Phase-based video motion processing. *ACM Transactions on Graphics (TOG)*, 32(4):1–10, 2013. [1](#), [2](#), [3](#), [6](#), [8](#), [9](#)
- [40] Neal Wadhwa, Michael Rubinstein, Frédo Durand, and William T Freeman. Riesz pyramids for fast phase-based video magnification. In *IEEE International Conference on Computational Photography (ICCP)*. IEEE, 2014. [1](#), [2](#)
- [41] Zhou Wang, Alan C Bovik, Hamid R Sheikh, and Eero P Simoncelli. Image quality assessment: from error visibility to structural similarity. *IEEE transactions on image processing*, 13(4):600–612, 2004. [7](#), [8](#)
- [42] Hao-Yu Wu, Michael Rubinstein, Eugene Shih, John Guttag, Frédo Durand, and William Freeman. Eulerian video magnification for revealing subtle changes in the world. *ACM transactions on graphics (TOG)*, 31(4):1–8, 2012. [1](#), [2](#), [3](#)
- [43] Yichao Zhang, Silvia L Pintea, and Jan C Van Gemert. Video acceleration magnification. In *IEEE Conference on Computer Vision and Pattern Recognition (CVPR)*, 2017. [2](#), [3](#)

Learning-based Axial Video Motion Magnification

Supplementary Material

Contents

A Implementation Details

- A.1 Data Generation
- A.2 Loss Function
- A.3 Projection Layer

B Additional Experiments

- B.1 Physical Accuracy
- B.2 Physical Accuracy of Axial Motion Magnification
- B.3 Motion Separation Effect of the MSM
- B.4 Angular Analysis of Axial Motion Magnification
- B.5 Per-pixel Motion Magnification

C Additional Results on Diverse Scenarios

Supplementary Material

In this supplementary material, we present the implementation details and additional experiments. Furthermore, we provide axial and generic motion magnification results across various scenarios.

A. Implementation Details

We provide the details of data generation pipeline (Sec. A.1), the loss function for the learning-based axial motion magnification (Sec. A.2) and the details of projection layer (Sec. A.3).

A.1. Data generation

Training Dataset. We randomly sample foreground textures ranging from 7 to 14 with segmentation masks from PASCAL VOC [10] and one background from COCO [19]. For each layer, we sample the axial magnification factor $\alpha = (\alpha^\phi; \alpha^{\phi_\perp})$ from the uniform distribution whose values are ranging from 1 to 80. Each element of translation parameter $\mathbf{d} \in \mathbb{R}^2$ is uniformly sampled from the range $-u$ to u , where $u = \min(10, 30/\max(\alpha^\phi, \alpha^{\phi_\perp}))$. It limits input motions to a maximum of 10 pixels or ensures amplified motions are kept under 30 pixels. We sample the angle ϕ within the range of 0 to 90 degrees. Note that our method enables axial motion magnification not only in the angle ϕ but also in the angle ϕ_\perp , thus facilitating axial motion magnification within the range of 0 to 180 degrees. To address the loss of subpixel motion due to image quantization, as proposed in DMM [24], we apply uniform quantization noise to the images before quantizing them.

Generic Evaluation Dataset. Based on the validation dataset of DMM [24], we construct the generic evaluation dataset comprising the previous image, next image, magnified image, and a single magnification factor. The generic evaluation dataset consists of two datasets for the subpixel test and noise test. The dataset for the subpixel test includes 15 levels of motion, ranging from a motion magnitude of 0.04 to 1.0 pixel, changing in a logarithmic scale. The motion magnification factor is adjusted to ensure that the amplified motion magnitude becomes 10 pixel. The dataset for the noise test includes 21 levels of noise, ranging from a noise factor of 0.01 to 100 in a logarithmic scale. The amount of input motion is 0.05 pixel, and the motion amplification factor is also set to ensure that the amplified motion magnitude becomes 10 pixel.

Axial Evaluation Dataset. The axial evaluation dataset consists of the previous image, next image, axially magnified image, axial magnification factor vector, and angle. The axial magnification factor vector is composed of two magnification factors corresponding to two orthogonal orientations. The axial evaluation dataset also includes two datasets for the subpixel test and noise test. For the subpixel test dataset, we generate data with 15 levels of motion ranging from 0.04 to 1.0 pixel in a logarithmic scale. We set the motion amplification factor vector to guarantee that the magnified motion magnitude along a random orientation equals 10 pixel. For the other orientation axis, we allocate half of that value. For the noise test dataset, we have 21 levels of noise factor ranging from 0.01 to 100 in a logarithmic scale. The input motion size along two orthogonal

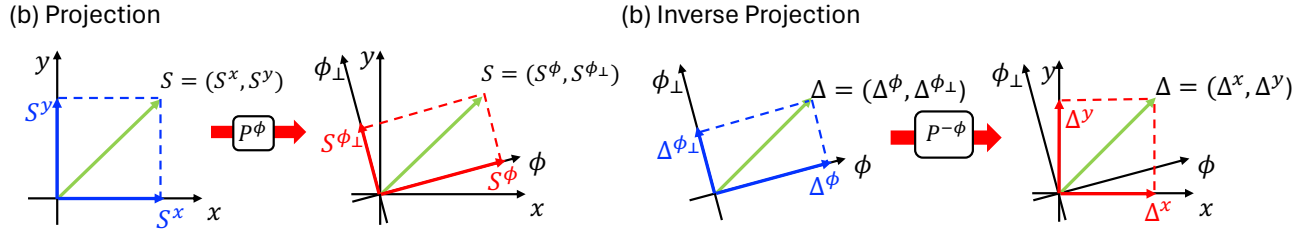
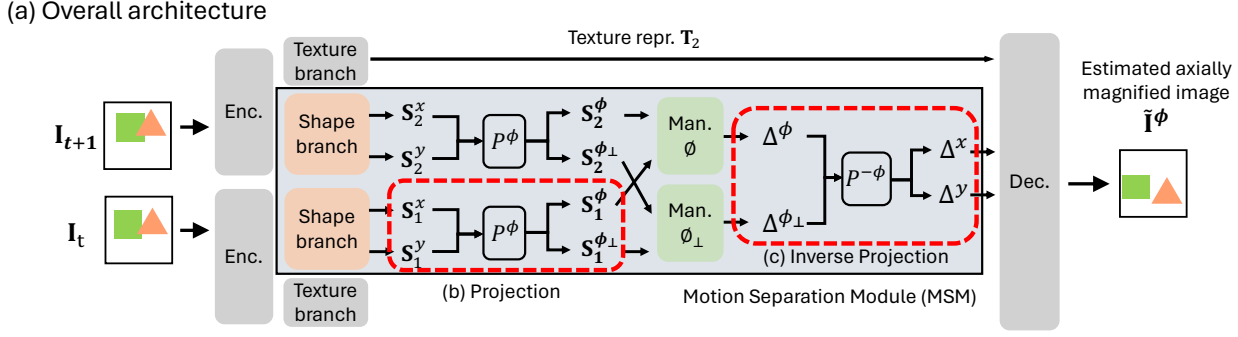


Figure 11. **Projection layer.** The projection and inverse projection layers facilitate the synthesis of arbitrarily rotated representations through a linear combination. In (a), the representations aligned with the x and y -axes undergo projection onto the ϕ and ϕ_{\perp} directions. Subsequently, in (b), these representations manipulated within the ϕ and ϕ_{\perp} directions before being projected back onto the x and y -axes.

orientations is 0.05 pixel, and the motion magnification factor is set to achieve an amplified motion size of 10 pixel for one of the orthogonal axes, while the motion magnification factor for the other axis is set to half of that value. The angle ϕ is randomly sampled between 0 and 90 degrees, except in the experiment of Fig. 5 in the main paper, where ϕ is set to the 0 degrees for comparison with the phase-based method [39].

A.2. Loss Function

DMM [24] proposes the texture loss L_{texture} and shape loss L_{shape} to represent intensity and motion information, respectively. These losses are combined with the reconstruction loss L_{recon} , forming the composite loss function of DMM. We slightly modify the loss of DMM to separately impose the loss to the x -axis and y -axis shape representations. The total loss function L_{total} is as follows:

$$L_{\text{total}} = L_{\text{recon}}(\hat{\mathbf{I}}^{\phi}, \tilde{\mathbf{I}}^{\phi}) + \beta(L_{\text{texture}}(\mathbf{T}_1, \mathbf{T}_2) + L_{\text{shape}}(\mathbf{S}_2^x, \hat{\mathbf{S}}_2^x)) + L_{\text{shape}}(\mathbf{S}_2^y, \hat{\mathbf{S}}_2^y), \quad (9)$$

where we set β to 0.5. We train our model using two NVIDIA Titan RTX GPUs.

A.3. Projection Layer

Motivated by the concept of steerable filters [13], we design the projection layer P^{ϕ} and inverse projection layer $P^{-\phi}$ using linear matrices. This enables the synthesis of arbitrarily rotated representations through a linear combination of directional representations. As shown in Fig. 11-(a), the axial shape representation along the canonical x and y -axes, which is induced by weight-shared 1D convolutions, are fed to the projection layer P^{ϕ} . With the linear operation, P^{ϕ} projects them and results in the axial shape representations of ϕ and ϕ_{\perp} directions. Conversely, the inverse projection layer $P^{-\phi}$ projects the outputs of the Manipulator $\Delta^{\phi}, \Delta^{\phi_{\perp}}$ back to the canonical x and y -axes (Fig. 11-(b)).

B. Additional Experiments

In this section, we assess the physical accuracy on generic motion magnification (Sec. B.1), the physical accuracy of the proposed axial motion magnification (Sec. B.2), motion separation effect of the MSM (Sec. B.3), and the behavior of our method across varying degrees (Sec. B.4). We also demonstrate the per-pixel motion magnification capability of our method (Sec. B.5).

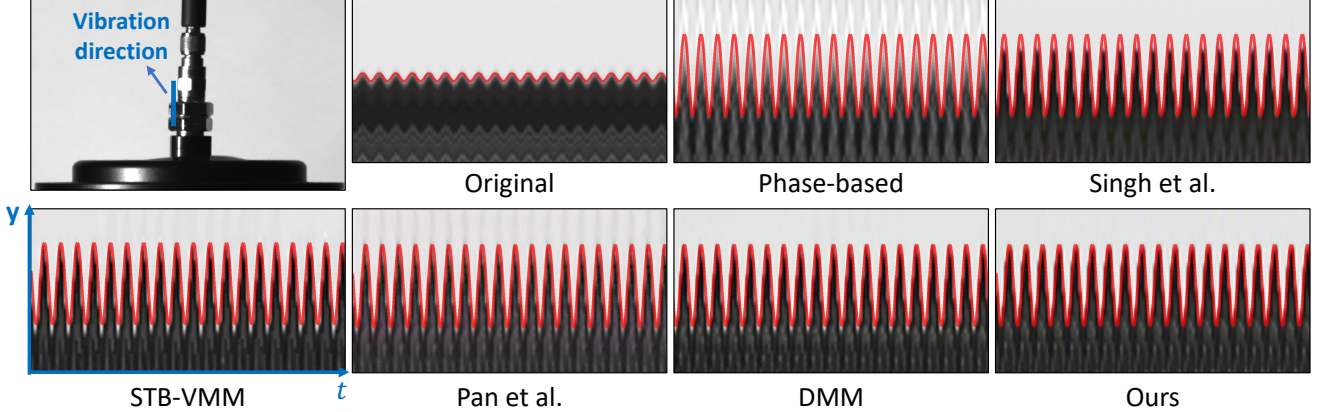


Figure 12. **Physical accuracy on generic motion magnification.** We compare the physically calculated sinusoidal wave of pixel displacement (red line) to the y - t slice’s waves of $10\times$ magnified videos from motion magnification methods. We also provide the y - t slice’s wave of the original video and sinusoidal wave before amplification for reference. The y - t slice’s wave of Ours matches the actual pixel displacement. The phase-based method [39] exhibits results consistent with the red wave of pixel displacement, albeit suffering from ringing artifacts. Other learning-based methods, such as DMM [24], STM-VMM [17], Pan *et al.* [26], and Singh *et al.* [31], also demonstrate correspondences, with a marginal difference in amplification.

Hyperparameters	Unit	Value
Vibration frequency ω	Hz	20
Peak amplitude of acceleration a	m/s^2	4.11
Camera-to-vibrator distance L	m	2
Focal length f	mm	100
Per-pixel sensor size v	μm	5.86

Table 1. **Hyperparameters for acquiring pixel displacement.**

B.1. Physical Accuracy on Generic Motion Magnification

To assess the physical accuracy of each method on generic motion magnification scenario, we examine whether the vibrations of the video which are magnified by each method match those of actual vibrations. First, we generate a 20Hz sinusoidal vibration using a vibration generator. Next, we obtain the peak amplitude of acceleration (m/s^2) from the attached accelerometer and convert it into a sinusoidal wave of displacement (m), which is transformed into a sinusoidal wave of pixel displacement (px) on the image plane through pinhole camera geometry. We investigate whether this wave corresponds to the vibration of the $10\times$ magnified video using the *static* mode. The transformation from the peak amplitude of acceleration a to the peak amplitude of displacement μ is as follows:

$$\mu = a/\omega^2, \quad (10)$$

where ω denotes the frequency of sinusoidal vibration. Using μ , we obtain the sinusoidal wave of real-world displacement $s(t)$ over time t and transform it into pixel displacement $k(t)$, which corresponds to

$$k(t) = \frac{f}{Lv} s(t). \quad (11)$$

The f , L , and v refer to the focal length, camera-to-vibrator distance, and per-pixel sensor size.

As shown in Fig. 12, the sinusoidal wave of our method demonstrates a correspondence with the red wave of pixel displacement that is $10\times$ amplified. The phase-based method [39] and other learning-based methods [17, 24, 26, 31] also exhibit correspondences, albeit with slight differences in amplification. These results validate the physical accuracy of our method, as well as that of other motion amplification methods. We provide the hyperparameters for converting acceleration (m/s^2) to pixel displacement (px) in Table B.1.

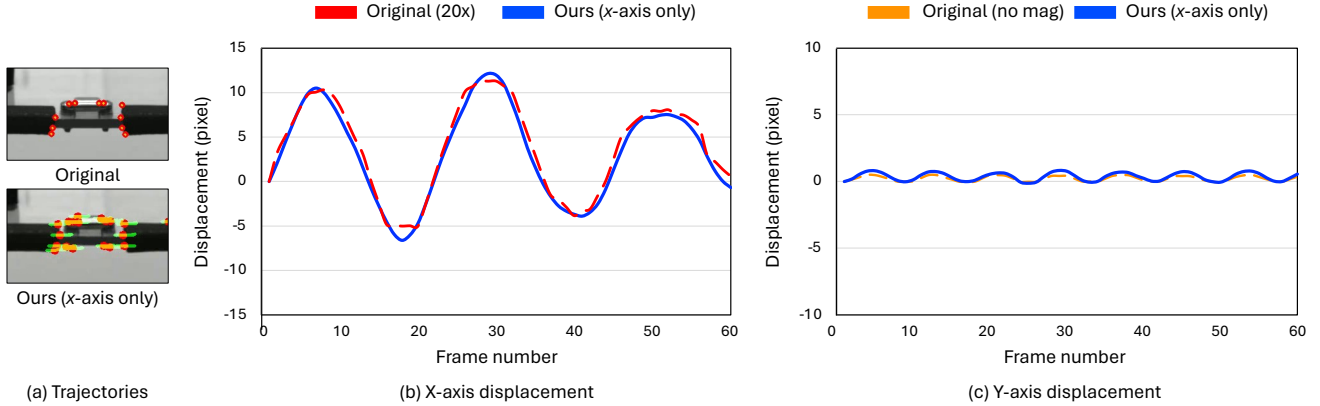


Figure 13. **Physical accuracy of the proposed axial motion magnification.** (a) Using the Kanade-Lucas-Tomasi (KLT) Tracker [21], we obtain the displacement values of the original video and the video which is $20\times$ amplified along x -axis by our method. (b) We multiply the x -axis' displacement value of the original trajectory by 20 and compare it with the x -axis' displacement value of the video which is amplified along x -axis by our method. (c) In the y -axis direction, we multiply the y -axis' displacement value of the original trajectory by 20 and compare it with the y -axis' displacement value of the video which is amplified along x -axis by our method.

B.2. Physical Accuracy of Axial Motion Magnification

We assess the physical accuracy of axial motion magnification when amplifying the motions, which move in various directions, into only the user-defined direction. As shown in Fig. 13-(a), utilizing the Kanade-Lucas-Tomasi (KLT) Tracker [21], we obtain the displacements of the original video and the video obtained from our method which is magnified 20 times along the x -axis. We evaluate both the physical accuracy and efficacy of axial motion magnification by comparing the displacement values from the trajectory of the video amplified $20\times$ using our method against the displacement values obtained by multiplying the original video's displacement values by 20. Figure. 13-(b) demonstrates the alignment between the trajectories of the video obtained by our method and the amplified original trajectory. For the y -axis displacement, the direction our method does not aim to amplify, the trajectory of the video obtained by our method aligns with the amplified original trajectory. (Fig. 13-(c)). These observations demonstrate that the proposed axial motion magnification not only preserves physical accuracy but also selectively amplifies motion along user-defined directions.

B.3. Motion Separation Effect of the MSM

We assess the effectiveness of the Motion Separation Module (MSM) in distinguishing between two orthogonal directional motions. To explore this, we rotate the video, where a vibrator oscillates solely along the y -axis, by the angle ϕ and apply the $10\times$ axial motion magnification to the video along the ϕ_{\perp} direction using both our method and the modified DMM with the *static* mode. Subsequently, we compare the time slices in the direction of ϕ_{\perp} , i.e., the direction with no motion. In this experiment, we set ϕ to 30 degrees. Figure 14 demonstrates the results. Unlike the ϕ_{\perp} - t slice of the original, where there is no motion in the ϕ_{\perp} direction, modified DMM fails to separate the motion and exhibits motion in the ϕ_{\perp} direction. In contrast, Ours with MSM effectively separates the motions in two orthogonal directions, showing results similar to the original in the ϕ_{\perp} direction.

B.4. Angular Analysis of Axial Motion Magnification

Our learning-based axial motion magnification can magnify the motion along the user-defined direction. We examine whether the behavior of our learning-based axial motion magnification remains consistent with changing angles. As shown in Fig. 15, we rotate the vibrator video at various angles ϕ and apply $10\times$ axial motion magnification to amplify only the motion corresponding to ϕ . Time slices are obtained from the lines that indicate identical positions across the various angle-adjusted videos. Then, the slices are sequentially connected over time. The connected time slices exhibit a smooth transition at boundaries where the angle ϕ changes. This demonstrates the consistent behavior of our learning-based axial motion magnification across various angles.

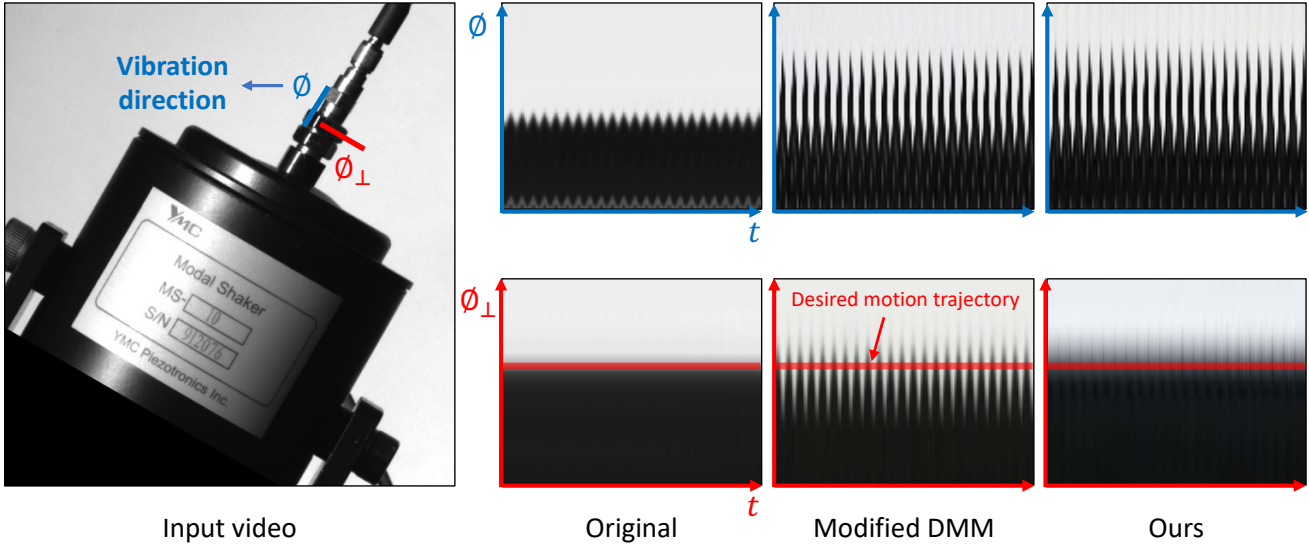


Figure 14. **Motion separation experiment with MSM.** Along the ϕ_{\perp} direction, we apply the $10\times$ axial motion magnification to the video of a vibrator oscillating only in the ϕ direction, using both our method and the modified DMM. Contrary to the ϕ_{\perp} - t slice of the original, the modified DMM exhibits vibration in the ϕ_{\perp} direction due to the unsuccessful motion separation. In comparison, our method, leveraging the proposed Motion Separation Module (MSM), successfully distinguishes between the two orthogonal motions, resulting in a ϕ_{\perp} - t slice that closely resembles the original's and desired motion trajectory, demonstrating the effectiveness of the MSM.

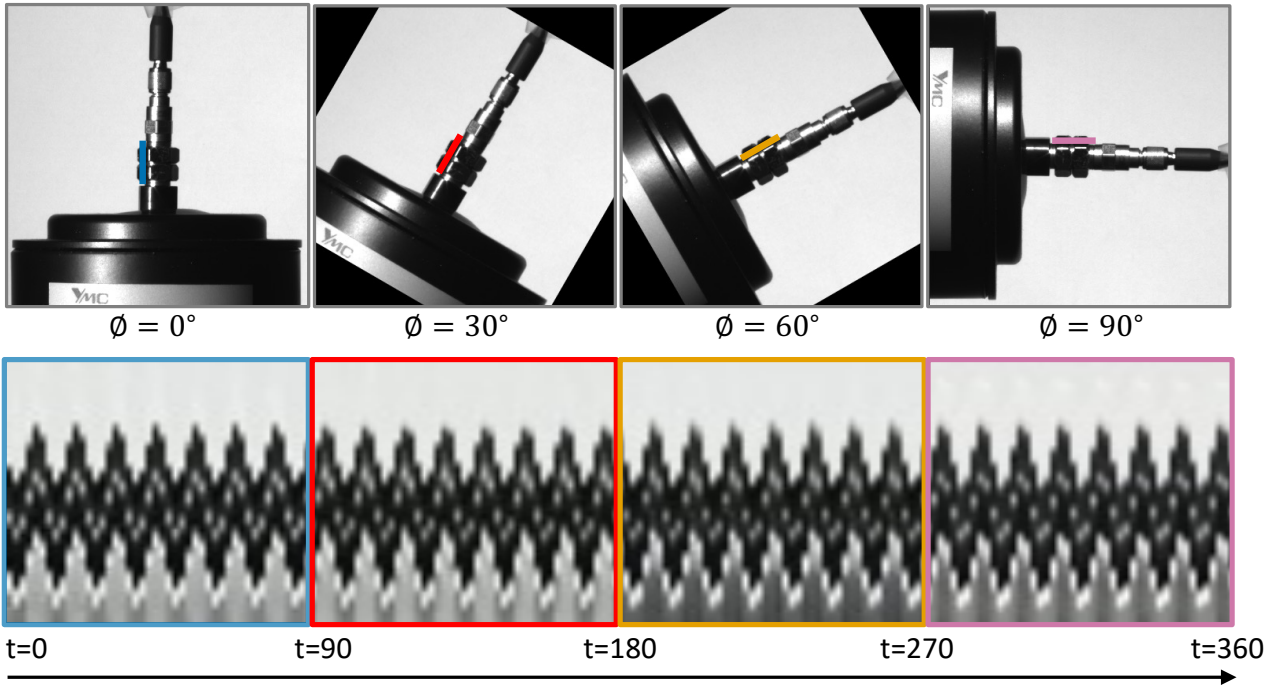


Figure 15. **Axial motion magnification results across various angles.** We applied axial motion magnification to amplify motion in the direction ϕ for vibrator videos rotated at various angles ϕ . The time slices of axially amplified videos using our method show the smooth transition at boundaries where the angle ϕ changes.

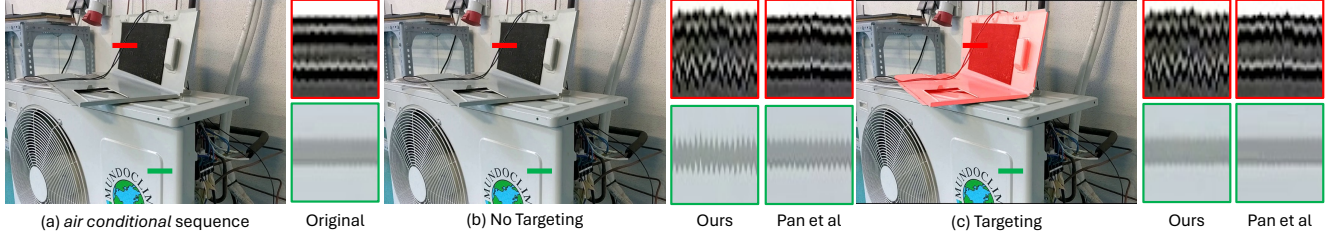


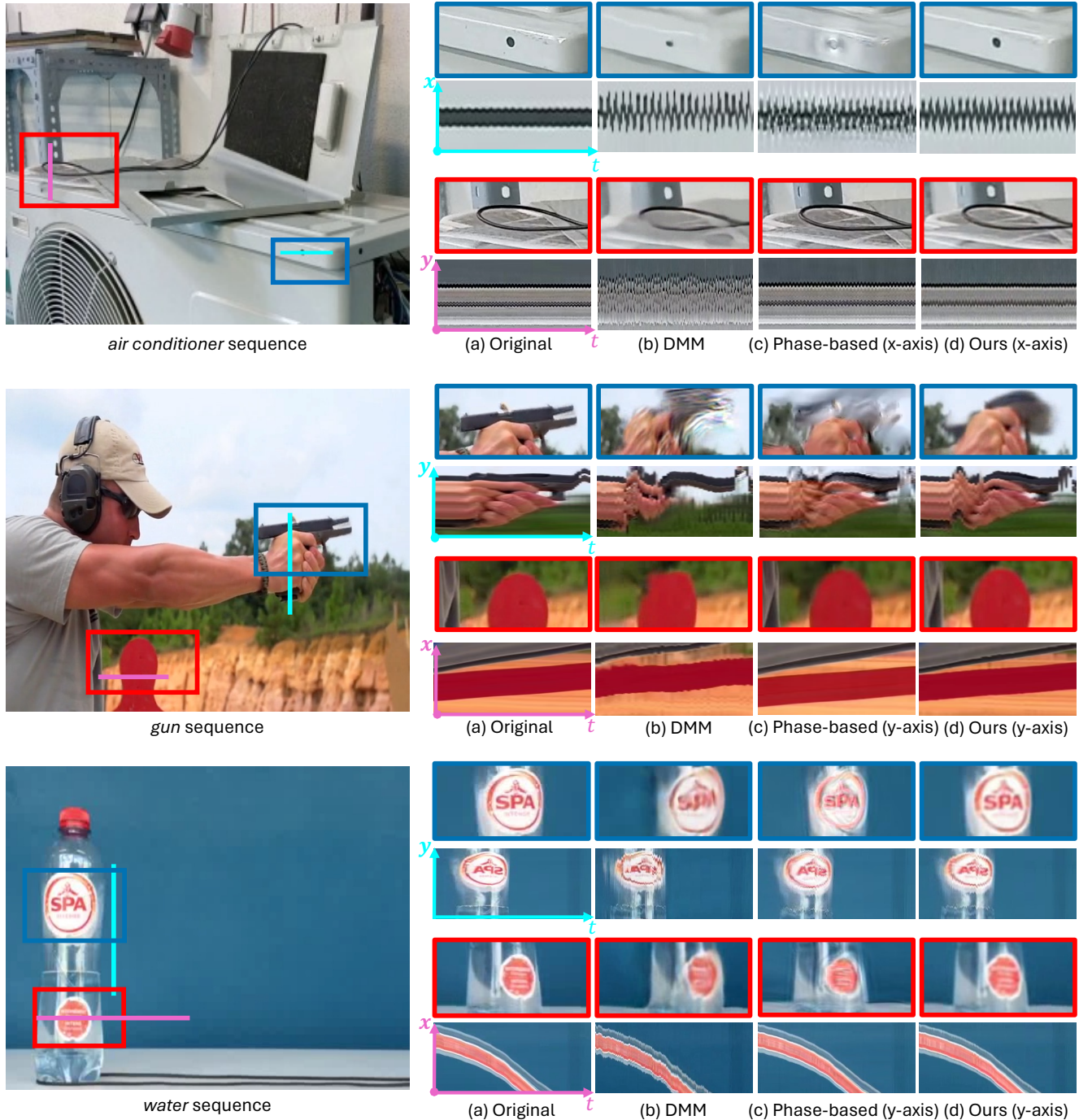
Figure 16. **Qualitative results of targeted motion magnification.** Our method is capable of per-pixel motion magnification because of the new proposed training dataset. To show this, Given a mask of the notebook, we selectively magnify the motion of the notebook using Ours and Pan *et al.* [26] When targeting the notebook for magnification, we observe that the motion of the air conditioner remains unchanged from the original, while only the motion of the notebook is amplified in Pan *et al.* and Ours.

B.5. Per-pixel Motion Magnification

During inference, our model demonstrates the ability to perform per-pixel motion magnification, which enables to vary magnification factors across different areas within an image. This capability is endowed by two main components: the angle ϕ and object-wise magnification map Λ , which are main parts of our newly proposed training dataset. We show this spatially selective motion magnification capability by presenting targeted results similar to those achieved by Pan *et al.* [26], which magnify specific objects within an image. Figure 16 displays the targeted motion magnification results of our method, alongside the targeted results obtained by Pan *et al.* When focusing on magnifying the motion of a notebook, we observe that the motion of the air conditioner remains unchanged from the original footage, while only the motion of the notebook is magnified in both Pan *et al.* and our method.

C. Additional Results on Diverse Scenarios

In this section, to demonstrate the efficacy of our approach, we present results from diverse scenarios. Our method is capable of both generic and axial motion magnification. Additionally, we observe that the learned shape representations are compatible with the temporal filter, similar to DMM [24]. Therefore, our proposed method provides four configurations based on the motion magnification approach and the application of temporal filters. The following figures demonstrate results on four distinct configurations: axial motion magnification without a temporal filter (Fig. 17), generic motion magnification without a temporal filter (Fig. 18), axial motion magnification with a temporal filter (Fig. 19), and generic motion magnification with a temporal filter (Fig. 20).

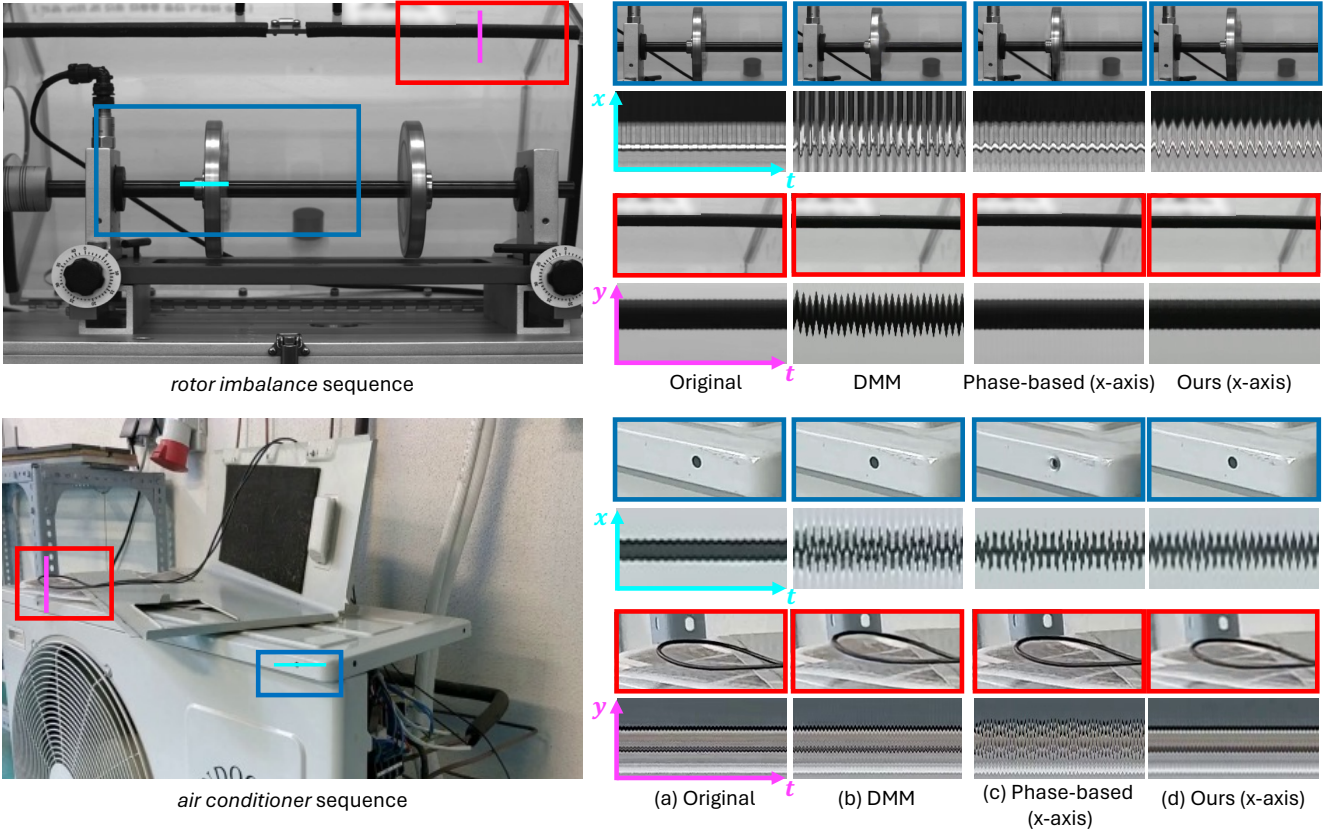


Sequence Name	Magnification factor	Mode
<i>air conditioner</i>	8	static
<i>gun</i>	8	dynamic
<i>water</i>	10	dynamic

Figure 17. **Qualitative results of axial magnification.** (a) Original: non-magnified. (b) DMM: magnified results with *generic* method [24]. We magnify x -axis motions in *air conditioner* and y -axis motions in *gun*, and *water* with (c) phase-based and (d) our methods respectively, plotting x - t and y - t slices for each of two different points. In **cyan** scenarios, where magnification aligns with the slice’s axis, ours presents less artifacts and clearer axial vibrations than phase-based, which suffers from severe artifacts and unclear vibrations. In **magenta** scenarios, when magnification is orthogonal to the slice’s axis, our method isolates motion effectively, preserving time slices similar to (a) without undesired magnification or artifacts. Conversely, DMM and phase-based struggle, leading to time slices deviating from the original, with notable artifacts.

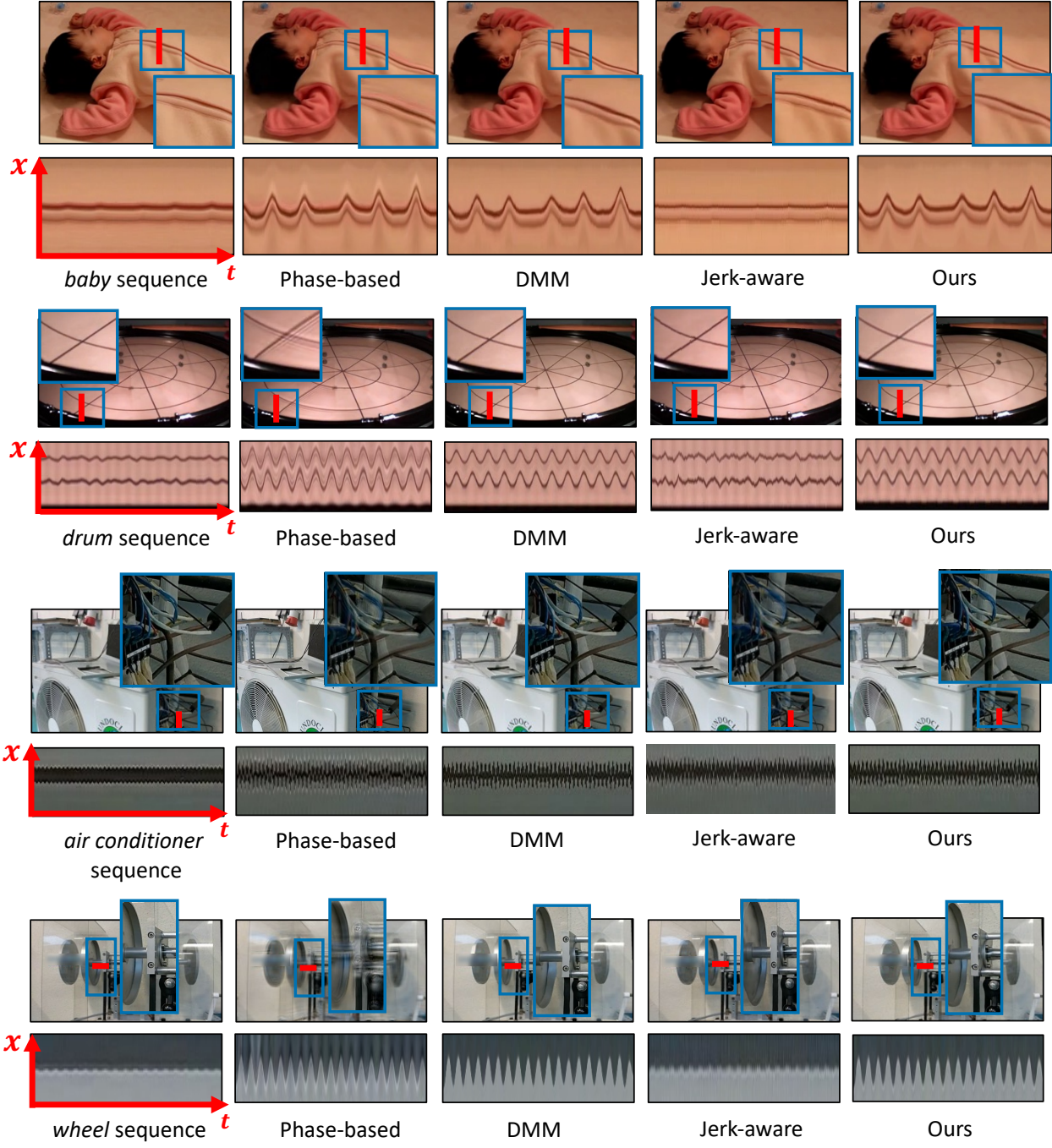


Figure 18. **Qualitative results of generic motion magnification.** We compare our method to the phase-based [39] method, Singh *et al.* [31], STB-VMM [17], Pan *et al.* [26], and DMM [24] in general motion magnification across various scenarios. Our method demonstrates clear magnified frames and the x - t slices.



Sequence Name	Magnification factor	FPS	Temporal Band	Temporal filter
<i>rotor imbalance</i>	40	120	0.04~0.4Hz	Butterworth
<i>air conditioner</i>	15	120	20~30 Hz	FIR

Figure 19. **Axial motion magnification with temporal filter.** With the temporal filters, we magnify the *rotor imbalance* and *air conditioner* sequences along the x -axis, *i.e.*, the axial direction, using (d) Ours and (c) phase-based method [39]. We also show the result of (b) DMM [24] with the temporal filter as one reference result of *generic* motion magnification methods. In **cyan** scenarios, where magnification aligns with the slice’s axis, ours shows less artifacts and legible axial vibrations. On the other hand, DMM and phase-based method both suffer from severe artifacts. In addition, DMM shows unclear vibration in the x - t slice, even with the temporal filter. In **magenta** scenarios, when magnification is orthogonal to the slice’s axis, our method effectively isolates the motions which are not aligned with the magnified direction, preserving time slices similar to (a) Original without undesired magnification or artifacts. Conversely, DMM in rotor imbalance sequence and phase-based in air conditioner sequence struggle to disentangle the unwanted motions, which leads to time slices deviating from the original and the magnified frames with artifacts and unclear axial vibrations.



Sequence Name	Magnification factor	FPS	Temporal Band	Temporal filter
<i>baby</i>	20	30	0.04~0.4Hz	Difference of IIR
<i>drum</i>	10	1900	74-78 Hz	FIR
<i>air conditioner</i>	15	120	20-30 Hz	FIR
<i>wheel</i>	20	120	20-30 Hz	FIR

Figure 20. **Generic motion magnification with temporal filter.** With temporal filters, we applied *generic* motion magnification to the *baby*, *drum*, *air conditioner* and *wheel* sequence using the phase-based, DMM [24], Jerk-aware [33] and our methods. Ours and DMM preserve the boundaries of the moving objects while depicting the motion well. The phase-based method exhibits slight ringing artifacts, and the Jerk-aware method shows the unstable separation of the motion signals.